Effect of a Low-Frequency Vortex on the Size of Typhoon Lan (2017)

MENGYUAN MA[a] AND TIM LI[a,b,c]

[a] *Key Laboratory of Meteorological Disaster, Ministry of Education (KLME)/Joint International Research Laboratory of Climate and Environmental Change (ILCEC)/Collaborative Innovation Center on Forecast and Evaluation of Meteorological Disasters (CIC-FEMD), Nanjing University of Information Science and Technology, Nanjing, China*

[b] *International Pacific Research Center, School of Ocean and Earth Science and Technology, University of Hawai'i at Mānoa, Honolulu, Hawaii*

[c] *Department of Atmospheric Sciences, University of Hawai'i at Mānoa, Honolulu, Hawaii*

(Manuscript received 17 June 2020, in final form 24 November 2020)

ABSTRACT: Typhoon Lan (2017) was one of the largest tropical cyclones (TC) in the western North Pacific Ocean (WNP), and it was developed in a low-frequency (10–90-day filtered) large-scale cyclonic vortex environment. The physical mechanism responsible for the TC's unusual size was investigated through idealized numerical experiments with the Weather Research and Forecasting Model. Sensitivity experiments showed that the low-frequency cyclonic circulation played an important role in modulating the TC size through the following three processes. First, it weakened the background vertical wind shear and provided a favorable condition for a more rapid growth of Lan. Second, it strengthened a vorticity aggregation process through enhanced background vorticity. As a result, a stronger and more organized TC core was quickly set up, which strengthened the TC intensity and expanded its size. Third, it enhanced the total surface wind speed and surface latent heat flux, strengthening convective instability in the outer region through increased moisture. The development of the outer rainband expanded the radial profile of diabatic heating, leading to greater low-level inflow and tangential wind acceleration in the outer region and thus a large TC size.

KEYWORDS: Tropical cyclones; Numerical analysis/modeling

1. Introduction

The size of a tropical cyclone (TC), defined as the azimuthal mean radius of 17 m s^{-1} surface tangential wind from the TC center (R17), is an important parameter to describe the TC structure and its impact area. A larger TC may readily modify its environmental flow (Carr and Elsberry 1997). In addition, a TC with a greater size leads to a greater destructive potential (Emanuel 2005; Sun et al. 2017). Irish et al. (2008) found that for a given TC intensity, the storm surge could change up to 30% within a reasonable TC size range. TCs tend to have a larger size and become more destructive under global warming (Sun et al. 2017).

Previous studies suggested that numerous factors such as latitude, ocean basin, environmental pressure, relative humidity, the distribution of diabatic heating and sea surface temperature might affect TC size (Atkinson 1971; Merrill 1984; Frank and Gray 1980; Weatherford and Gray 1988; Cocks and Gray 2002; Liu and Chan 2002; Kimball and Mulekar 2004; Hill and Lackmann 2009; Chavas and Emanuel 2010; Chan and Chan 2012; Knaff et al. 2014; Frisius 2015; Tsuji et al. 2016; Sun et al. 2017). For instance, Holland and Merrill (1984) found that the size of a TC was affected by its interaction with the environmental flow. Liu and Chan (2002) emphasized the role of synoptic flow patterns in affecting TC size. Hill and Lackmann (2009) suggested that environmental relative humidity is an important factor affecting TC size. Ma et al. (2019) noted that the difference of TC size between the western North Pacific (WNP) and the North Atlantic depended primarily on the distinctive vertical temperature profiles of the mean state over the two basins. Smith et al. (2011) suggested that an optimum background rotation strength existed for TC size. Several idealized numerical model experiments indicated that the final size of a TC depended on initial vortex radial distribution (e.g., Rotunno and Emanuel 1987; Xu and Wang 2010a,b; Chan and Chan 2014; Kilroy and Smith 2017). Initial larger horizontal wind extent and higher wind speed outside the inner core favored the vortex expansion in the later development stage (Chan and Chan 2014; Kilroy and Smith 2017).

Typhoon Lan was the largest TC over the WNP in 2017. Compared to the median size of 185 km in the WNP (see Table 1 of Ma et al. 2019), TC Lan reached a maximum size of 447 km at 0300 UTC 21 October 2017. What caused such an unusually large TC size? Motivated by this question, we examined the evolution of the low-frequency background circulation and the typhoon. Figure 1 shows the evolution of the vertically integrated 10–90-day-filtered horizontal wind and outgoing longwave radiation (OLR) fields from 17 to 22 October 2017. A Lanczos bandpass filter (Duchon 1979) with a 10–90-day period was performed to the reanalysis data around the TC period to extract the low-frequency signal. This method modifies the response function by adjusting weight functions so that the amplitude of Gibbs oscillation is reduced. The difference between the unfiltered field and the filtered field with the 10–90-day bandpass filter represents the lower-frequency background mean flow and the synoptic-scale flow that includes initial TC vortex. It is interesting to note that during its northward journey, Typhoon Lan was always embedded in a large-scale

Corresponding author: Tim Li, timli@hawaii.edu

DOI: 10.1175/MWR-D-20-0200.1

TABLE 1. List of the control experiment and all sensitivity experiments.

Expt name	Description
CTL	Total fields from NCEP FNL are specified in the initial and lateral boundary conditions
NO_ISO	As in CTL except that all of the intraesasonal fields are removed from the initial and lateral boundary conditions
NO_SH	As in CTL except that only the intraseasonal moisture field is removed from the initial and lateral boundary conditions
NO_V	As in CTL except that only the intraseasonal wind related (including temperature and pressure) fields are removed from the initial and lateral boundary conditions

background cyclonic vortex. The zonal scale of the large-scale vortex was around 4000 km.

The WNP is the active region of the atmospheric intraseasonal oscillation (ISO) and synoptic-scale variability (Li and Wang 2005; Zhou and Li 2010). TC development in the WNP is often accompanied by multiscale low-frequency waves including the ISO (Liebmann et al. 1994; Maloney and Hartmann 1998; Fu et al. 2007; Li 2012; Li and Zhou 2013a,b; Li 2014). The ISO exerts a large-scale control on TCs and is one of the vital factors affecting TC genesis (Xu et al. 2013, 2014; Cao et al. 2014; Zhao and Li 2018), rapid intensification (Hsu et al. 2011; Yan et al. 2019), and movement (Bi et al. 2015; Yang et al. 2015). As a typical low-frequency circulation in the WNP, the monsoon gyre (MG) has a marked impact on TC formation (Lander 1994; Harr et al. 1996; Ritchie and Holland 1999; Li et al. 2006; Wu et al. 2013). Based on high-resolution numerical model simulations, Bi et al. (2015) demonstrated that there was a two-way interaction between TC Megi (2010) and a low-frequency MG.

Previous studies of the TC–ISO relationship mostly focused on the impact of the ISO on TC genesis and track. Less attention was paid to the effect of the low-frequency circulation on TC size. The objective of the present study is to investigate specific physical processes through which the low-frequency circulation influenced the size of TC Lan (2017). The remaining part of this paper is organized as follows. section 2 provides a brief overview of TC Lan and the surrounding low-frequency circulation. The numerical experiment design is given in this section as well. section 3 describes the model control simulation result. In section 4, the relative contribution of the low-frequency dynamic (wind) and thermodynamic (moisture) fields are examined with sensitivity experiments. In section 5, the specific mechanism responsible for the impact of the low-frequency circulation on the TC size is discussed. Conclusions and discussion are given in section 6.

2. Overview of TC Lan and experiment design

Supertyphoon Lan formed in the WNP on 15 October 2017, initially as a tropical depression. It moved into the Philippine Sea and became a named tropical storm, Lan, by 0000 UTC 16 October. After its genesis, Lan moved toward the north and had rapidly intensified into a typhoon at 0000 UTC 18 October and its size was only about 160 km at that time. After this, Lan expanded in size and continued to develop while moving northward. At 1800 UTC 20 October, the typhoon underwent rapid intensification and its R17 grew into 400 km, reaching the supertyphoon intensity. Though the TC was headed on a northward track, its outer bands reached as far as Taiwan and the Philippines, which were about 1100 km from the TC center. Farther north to the east of Taiwan, Lan reached its peak intensity at 1200 UTC 21 October, with a central minimum sea level pressure of 922 hPa and a maximum sustained wind speed of 67 m s^{-1}. It is noted that Lan's size is calculated by the Multiplatform Tropical Cyclone Surface Wind Analysis (MTCSWA; Knaff et al. 2011) data, which is the high-resolution storm-centered wind dataset for individual TCs.

To investigate the effect of the low-frequency cyclonic vortex on the large size of TC Lan, we design the following control and sensitivity experiments. The numerical model used in this study is version 3.7.1 of the Advanced Research core of the Weather Research and Forecasting (WRF-ARW) Model (Skamarock et al. 2008) with three interactive nested domains. The mesh sizes in the three domains are 300 × 250, 301 × 301, and 301 × 301 with horizontal grid sizes of 27, 9, and 3 km, respectively. The model has 47 vertical levels with the top at 10 hPa. The National Centers for Environmental Prediction (NCEP) global final (FNL) analysis was used to provide the model initial and lateral boundary conditions. The Kain–Fritch convective scheme (Kain and Fritsch 1993) is used in the two outermost meshes, whereas the convection is explicitly resolved in the innermost mesh. The other model physics include WSM 6-class cloud microphysics scheme (Hong and Lim 2006), the Dudhia for shortwave radiation (Dudhia 1989), the Rapid Radiative Transfer Model (RRTM) for longwave radiation scheme (Mlawer et al. 1997), the Yonsei University (YSU) planetary boundary layer scheme (Hong et al. 2006), and Monin–Obukhov surface-layer scheme (Beljaars 1995). The surface bulk drag (Charnock 1955) is applied in all the model domains. The observed lateral boundary condition from the NCEP final analysis (FNL) is specified in the outermost domain. Two inner nested domains move automatically following the model storm (Davis et al. 2008).

In the control experiment (CTL), the model initial condition is specified from the NCEP FNL at 0000 UTC 17 October 2017, and it is integrated for 4 days. In the sensitivity experiment (NO_ISO), the 10–90-day-filtered ISO fields including wind, temperature, specific humidity, geopotential height and sea level pressure are removed from the initial and lateral boundary conditions of the NCEP FNL dataset. By comparing the CTL and NO_ISO experiments, one may reveal how and to what extent the low-frequency cyclonic MG affects the TC size.

Two additional sensitivity experiments are further carried out, to understand the relative roles of the low-frequency wind and moisture fields in modulating the TC size. In the NO_SH experiment, only the 10–90-day-filtered

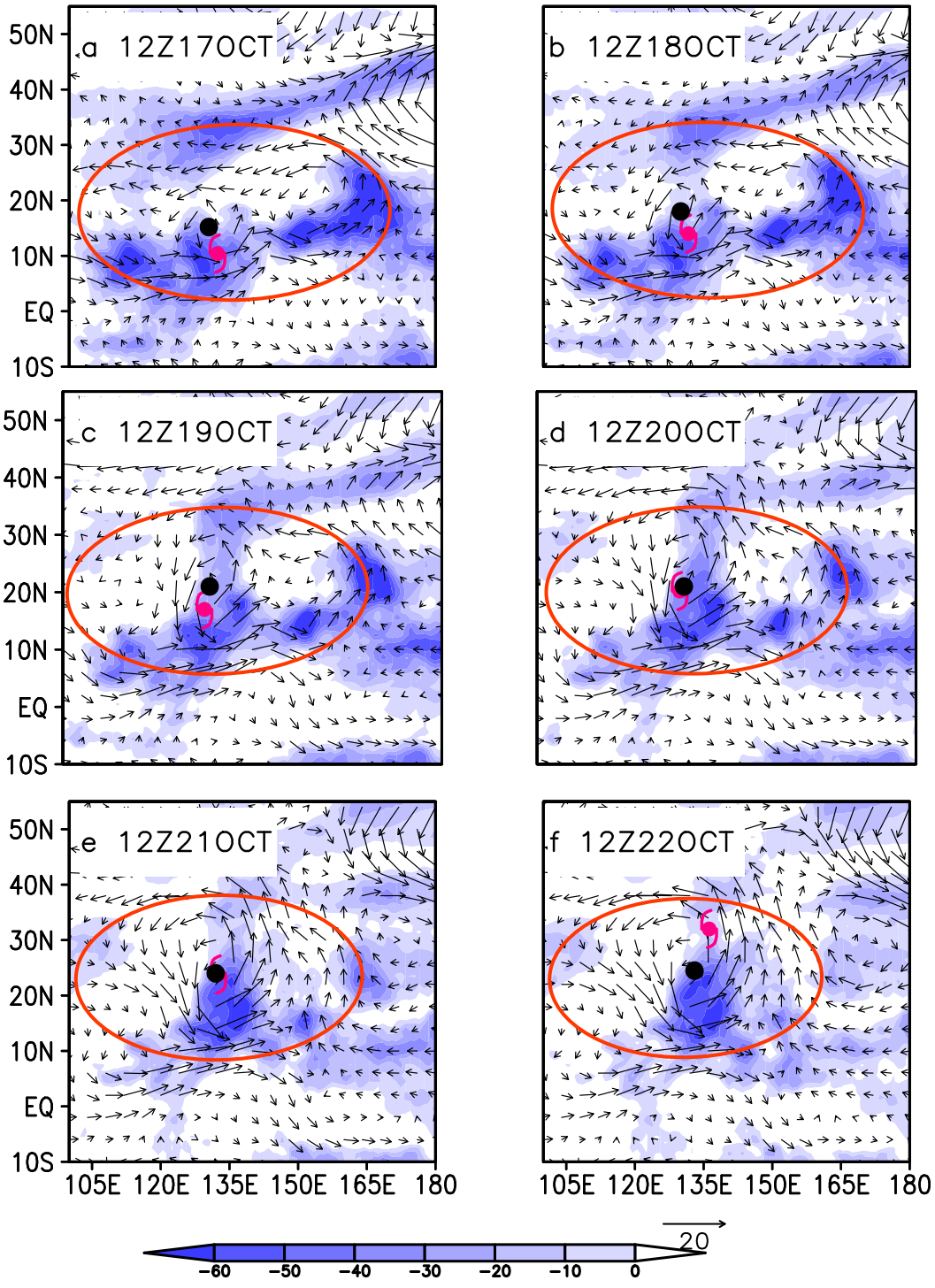

FIG. 1. Evolution of 10–90-day bandpass-filtered wind field (vectors) averaged between 850 and 300 hPa and OLR field (shaded; W m^{-2}). The red oval shows the approximate shape of the 10–90-day low-frequency vortex. The black dots and red typhoon marks represent the centers of the low-frequency vortex and the TC Lan, respectively.

specific humidity anomaly field is removed from the initial and lateral boundary conditions, while the other low-frequency variables such as the wind, geopotential height and temperature field are retained so that the background dynamic fields remain in hydrostatic and quasigeostrophic balance. This experiment is designed to investigate the sole effect of the low-frequency moisture on the TC size. In contrast, the NO_V experiment retains only the low-frequency moisture

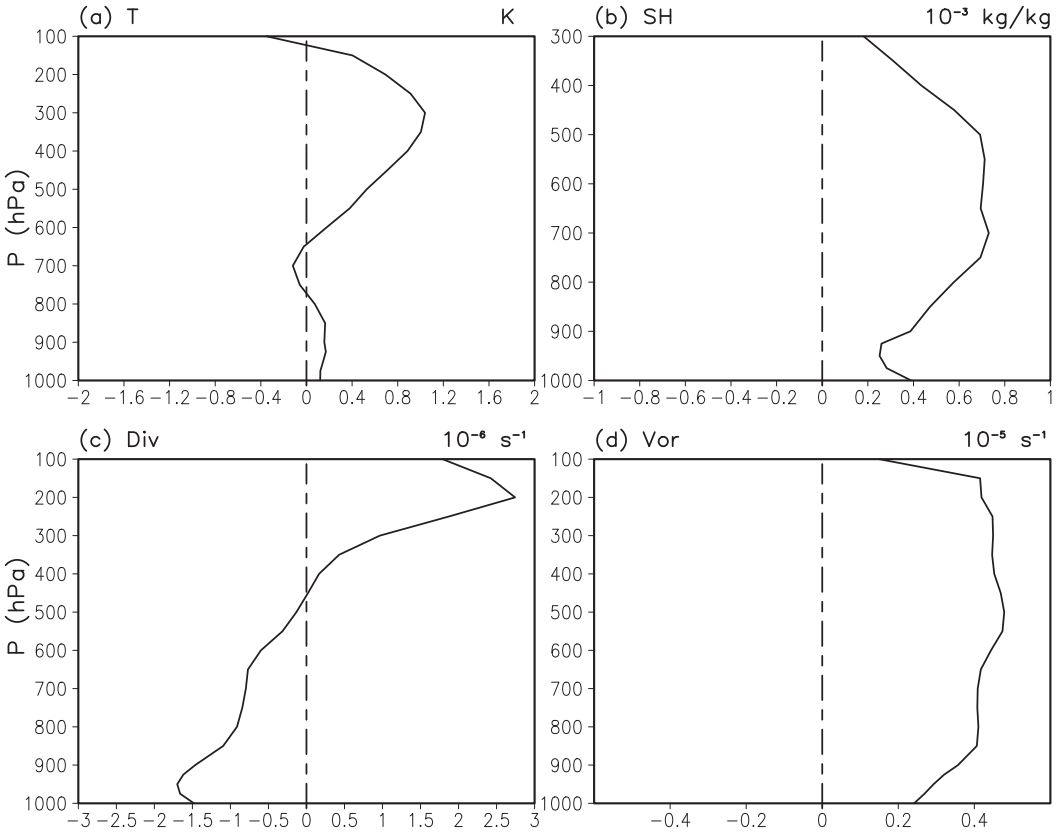

FIG. 2. The vertical profiles of area-averaged (5°–30°N, 110°–170°E) (a) temperature, (b) specific humidity, (c) divergence, and (d) vorticity fields associated with the low-frequency circulation at the model initial time.

field while removing the other low-frequency fields. By comparing the TC size difference between the NO_SH and NO_V experiments, one may reveal the relative contribution of the dynamic and thermodynamic impact on the TC size. Table 1 lists the control and all the sensitivity experiments.

3. Distinctive TC sizes simulated by the CTL and NO_ISO

As described in the previous section, the control and NO_ISO sensitivity experiments are designed to investigate the role of the large-scale ISO flow on the TC size. As the TC was surrounded by the large-scale ISO flow, we first plotted the vertical profiles of area-averaged (5°–30°N, 110°–170°E) low-frequency temperature, specific humidity, divergence and vorticity fields (Fig. 2). The temperature vertical profile shows a higher temperature anomaly in the upper troposphere (200–300 hPa) than in the lower troposphere, inferring a more stable stratification associated with the ISO (Fig. 2a). The specific humidity profile presents positive anomalies throughout the troposphere (Fig. 2b). Such a moisture profile is consistent with a convergence anomaly in the lower troposphere, a divergence anomaly in the upper troposphere (Fig. 2c), and an ascending anomaly in the midtroposphere due to the mass continuity. A pronounced positive vorticity anomaly occurs throughout the troposphere (Fig. 2d). This background deep-layer vorticity, along with the positive moisture anomalies, may contribute greatly to the unusual large size of TC Lan.

The average radius of 17 m s^{-1} surface tangential wind speed (R17) is used to measure the TC size. Figure 3 shows the observed and simulated TC tracks and time evolutions of the minimum sea level pressure (MSLP) and the TC size (R17) from the observation and the CTL experiment. The CTL simulation is able to capture the observed TC track, MSLP and R17 (Figs. 3a–c) even though the maximum surface wind speed (MWS) is underestimated slightly after hour 72 (not shown). At hour 96, the simulated TC size in the CTL experiment is about 430 km, close to the observed.

Figure 4 shows the simulation results from the CTL and NO_ISO experiments. An obvious difference is the simulated TC size at hour 96. The R17 difference between the two experiments becomes larger and larger with time integration (Fig. 4b). At hour 96, the TC size in the NO_ISO experiment is only about a half of that in the CTL experiment. In contrast to the steady increase of the size difference, the TC intensity evolutions appear more complicated. A common feature among the MWS and MSLP evolutions is a weaker intensity in NO_ISO relative to CTL during the initial 72-h integration period.

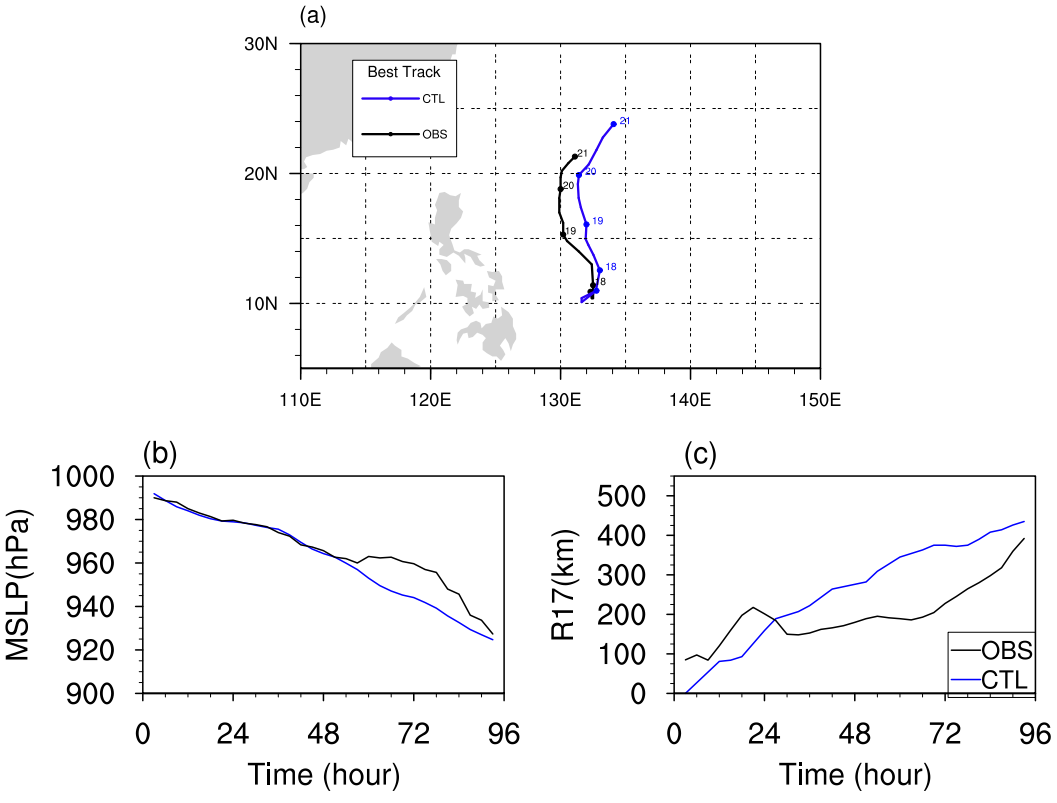

FIG. 3. (a) The JTWC best track (black) and the simulated Lan track in the control experiment (blue) from 0000 UTC 17 Oct to 0000 UTC 21 Oct at 24-h intervals. Time series of (b) the minimum sea level pressure (hPa) and (c) R17 (km; representing TC size) from MTCSWA (black) and the control experiment (blue) correspond to the above time.

The TC size difference may be better viewed from the horizontal distribution of the simulated 850-hPa wind fields (Fig. 5). Note that the TC cyclonic circulation in the CTL experiment is stronger, starting from the initial condition, and develops at a much faster rate. The cyclonic circulation expands rapidly toward the outer region. In contrast, the cyclonic circulation is weaker and confined in the inner core region as a result of the absence of the low-frequency ISO flow in NO_ISO.

The dependence of the TC size on initial TC intensity may be further viewed from the radial profiles of azimuthal-mean tangential wind fields (Fig. 6). At least for the first 72 h, the radial slope of the tangential wind in the outer region appears fixed. As a result, the expansion of the TC size is closely related

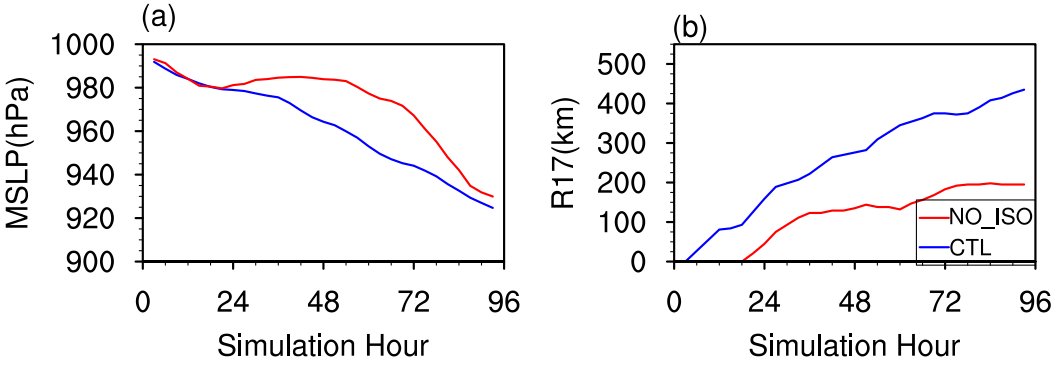

FIG. 4. Time series of (a) the minimum sea level pressure (hPa) and (b) R17 (km) for the control experiment (blue) and the NO_ISO experiment (red).

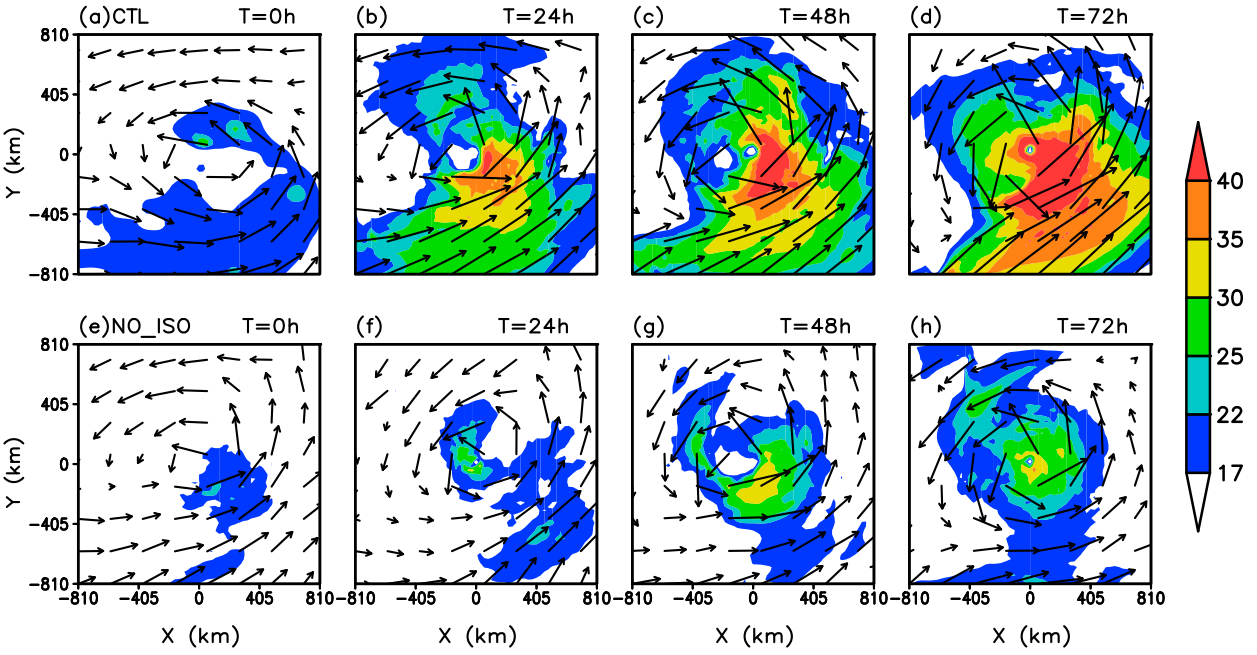

FIG. 5. Simulated wind field (vectors) and total wind speed (shaded) at 850 hPa in (a)–(d) CTL and (e)–(h) NO_ISO at a time interval of 24 h.

to the increase of the TC intensity. A more general relationship between the TC intensity and size will be discussed in section 5.

The numerical model simulations above successfully illustrate the role of the low-frequency circulation in affecting the TC size. Given that the low-frequency mode contains both the dynamic (wind) and thermodynamic (moisture) fields, in the following section we further investigate their relative roles.

4. Relative roles of low-frequency dynamic and thermodynamic fields

To reveal the relative roles of the low-frequency dynamic and thermodynamic fields, we conducted two additional sensitivity experiments. Figure 7 shows the time evolutions of simulated MSLP and R17 in NO_SH and NO_V, respectively. As compared with the CTL experiment, the TC size in the two additional sensitivity experiments shows a distinctive feature. In NO_SH, the TC size differs greatly during the initial 24-h period compared to CTL, and the size difference decreases with time (Fig. 7b). In contrast, the TC size difference between NO_V and CTL is small initially and increases greatly with time (Fig. 7d).

To quantitatively describe the TC size difference between NO_SH and NO_V, we introduce a size index, defined as the time average of R17 difference from the CTL experiments during hours 24–96 (shown in Figs. 7b and 7d). Figure 8 illustrates the calculated size index in NO_ISO, NO_V and NO_SH. It indicates that the TC size change is much greater in NO_V (162.5 km) than in NO_SH (60.3 km). This corresponds to 73% and 27% of the size change by the dynamic and moisture fields, respectively. Therefore, the low-frequency wind field plays a dominant role in regulating the TC size change.

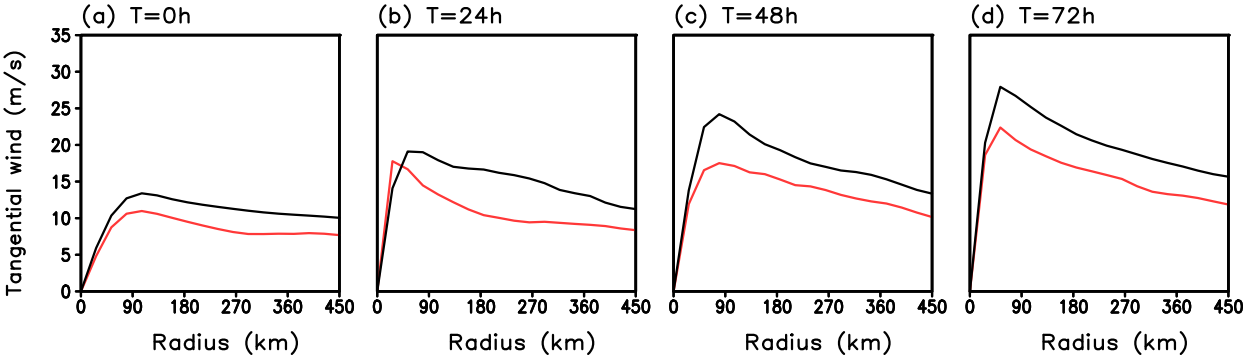

FIG. 6. The radial distribution of the azimuthal-mean tangential wind profile at 10 m for the CTL (black) and NO_ISO (red) experiments.

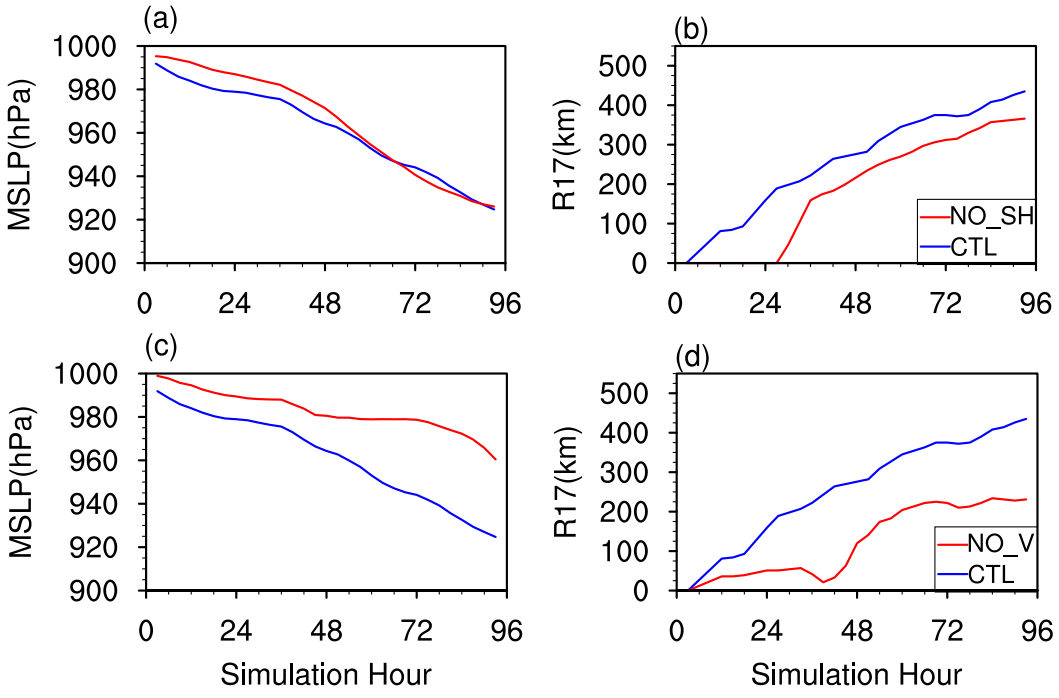

FIG. 7. Time evolutions of (left) the TC minimum sea level pressure (hPa) and (right) R17 (km; representing the TC size) for the (a),(b) NO_SH and (c),(d) NO_V experiments.

The size difference between NO_V and NO_SH is accompanied by the intensity difference shown in Figs. 7a and 7c. Note that the simulated MSLP in NO_SH is quite close to that in CTL, whereas the simulated MSLP in NO_V is much weaker. This implies a connection between the TC intensity and R17. A stronger TC intensity leads to a greater TC size. This result is consistent with that shown in Fig. 6.

Because the TC size difference is most obvious in NO_V (Fig. 7d) compared to CTL, in the next section we will focus on examining the difference between NO_V and CTL. A special attention will be paid to the impact of the low-frequency wind on the TC size.

5. Impact of the low-frequency wind on TC size

A key question is how the low-frequency dynamic field can substantially affect TC size. We hypothesize that it may work through the following three processes. The first is through its impact on the background vertical wind shear (VWS). Strong VWS generally has a negative impact on the TC intensification (e.g., Gray 1968; DeMaria and Kaplan 1994; Wang and Holland 1996; Jones 1995, 2000; Hanley et al. 2001). A greater intensity often leads to a greater TC size (Wu et al. 2015; Knaff et al. 2016; Ma et al. 2019). Therefore, we first examine the background VWS fields in the CTL and NO_V experiments.

Figure 9 shows the area-averaged vertical wind shear vector around the initial TC center. It was calculated based on a region with a radius of 400 km centered at the TC center. The black arrow represents the VWS of the low-frequency field, the purple arrow is the VWS in CTL, and the green arrow represents the VWS in NO_V. Therefore, the background VWS is weaker in CTL, whereas it becomes stronger in NO_V. The calculated VWS for the total wind in CTL is 4.0 m s^{-1}. The

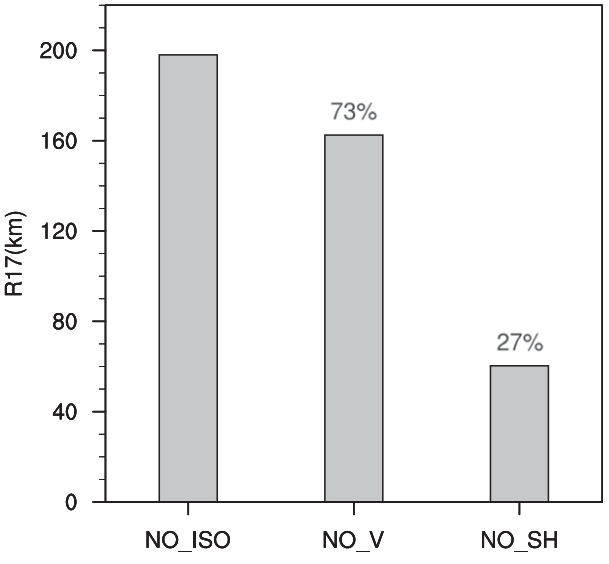

FIG. 8. Relative contribution of the low-frequency dynamic and thermodynamic impact on the TC size. The left bar shows the R17 difference between CTL and NO_ISO. The center bar shows the R17 difference between CTL and NO_V. The right bar shows the R17 difference between CTL and NO_SH.

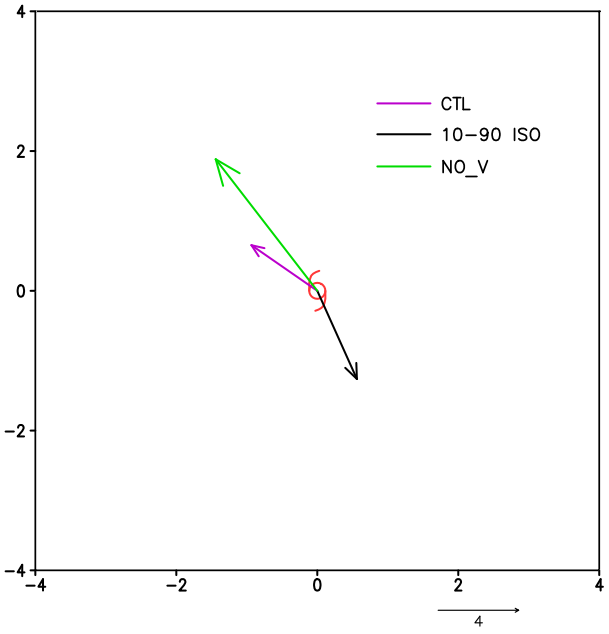

FIG. 9. Area-averaged vertical wind shear (m s^{-1}) within a radius of 400 km centered on the TC center at the model initial time. The black, purple, and green arrows denote the VWS of the low-frequency flow, the total flow in CTL, and the flow with the low-frequency motion removed in NO_V, respectively.

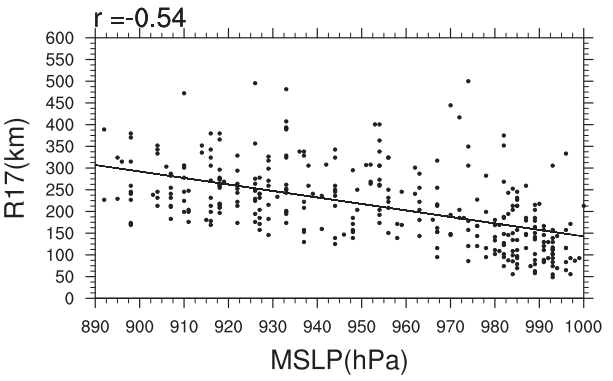

FIG. 10. Scatter diagram of MSLP (hPa) vs R17 (km) during the time of the maximum TC intensity in the WNP derived from the JTWC best track dataset during 2001–18. The correlation is statistically significant at a 99% confidence level.

VWS associated with the low-frequency vortex is 4.8 m s^{-1}, and the VWS in NO_V is 8.3 m s^{-1}.

According to Nolan and McGauley (2012), a light wind shear (2.5–5 m s^{-1}) is favorable for TC development, whereas a larger wind shear value (>7.5 m s^{-1}) hinders TC development. The result is consistent with that derived from the current sensitivity experiments. In CTL when the initial TC vortex develops within the low-frequency circulation, the VWS is in the range of the light wind shear, which favors the TC development. In NO_V when the low-frequency flow is removed, the VWS becomes much larger and is in the range of the larger wind shear, which is not conducive to a strong TC development. The result implies that the low-frequency VWS tends to weaken the seasonal mean background vertical shear and thus provides a favorable condition for the TC development. A greater TC intensity may further lead to a larger TC size.

To examine a statistical relationship between TC intensity and size over the WNP, we plotted a scatter diagram between them during 2001–18 in Fig. 10. Here TC intensity is represented by MSLP whereas TC size is represented by R17. Both the MSLP and R17 are from the Joint Typhon Warning Center (JTWC) dataset. Total typhoon numbers examined during the period is 334. For each typhoon, the MSLP and R17 during the time of its maximum intensity are used in the scatter diagram. The correlation coefficient between the MSLP and R17 is −0.54, which is statistically significant, exceeding a 99% confidence level. Therefore, a stronger TC in general possesses a larger size in the WNP.

The second process is through the vorticity aggregation process. The low-frequency flow exhibits a cyclonic vorticity anomaly throughout the troposphere (Fig. 2d). The enhanced background cyclonic vorticity tends to force convective instability generated small-scale vortical hot towers (VHTs) toward the TC center (Nolan 2007; Montgomery et al. 2012; Davis 2015; Kilroy and Smith 2016). Figure 11 depicts the evolutions of the relative vorticity field at 900 hPa in CTL and NO_V. At hour 12, a large number of small-scale convective cells (represented by small-scale vorticity centers) appear in the outer region, due to enhanced surface latent heat flux (Li 2012). Compared with the background without the low-frequency vortex, the enhanced background cyclonic vorticity in CTL forces the small-scale VHTs to move toward the TC center more efficiently through the vorticity segregation process. As these positive vorticity eddies move radially inward and become closer to each other, they have great potential to merge, forming a stronger mesoscale core. As a result, a stronger and larger TC core forms at hours 24 and 48 in CTL (Fig. 11). This self-aggregation feature is similar to previous studies (e.g., Ge et al. 2013a; Ge et al. 2015). Therefore, the low-frequency background vorticity, through the vorticity segregation process, leads to a faster growth of the TC intensity in CTL than in NO_V. The overall impact of the low-frequency vorticity is to merge small-scale unorganized convective cells into an organized TC core system.

It is worth mentioning that a recent study by Kilroy et al. (2017) found that the classical barotropic vorticity segregation dynamics involving the inward movement of cyclonic vorticity anomalies and the expulsion of anticyclonic anomalies were not clearly presented in a full-physics model. In particular, anticyclonic anomalies were difficult to be "pushed away" as they were embedded in a layer of strong inflowing air. Rather, in an environment with increased background cyclonic vorticity as in the CTL case, individual convective cells produced much stronger positive vorticity anomalies than anticyclonic anomalies, because a positive circulation–convection feedback happened only in the cyclonic vorticity regions. The cells were stretching locally the strong background rotation. In the end the anticyclonic anomalies produced by tilting were relatively weak and shorter lived than the cyclonic anomalies (Kilroy and Smith 2016).

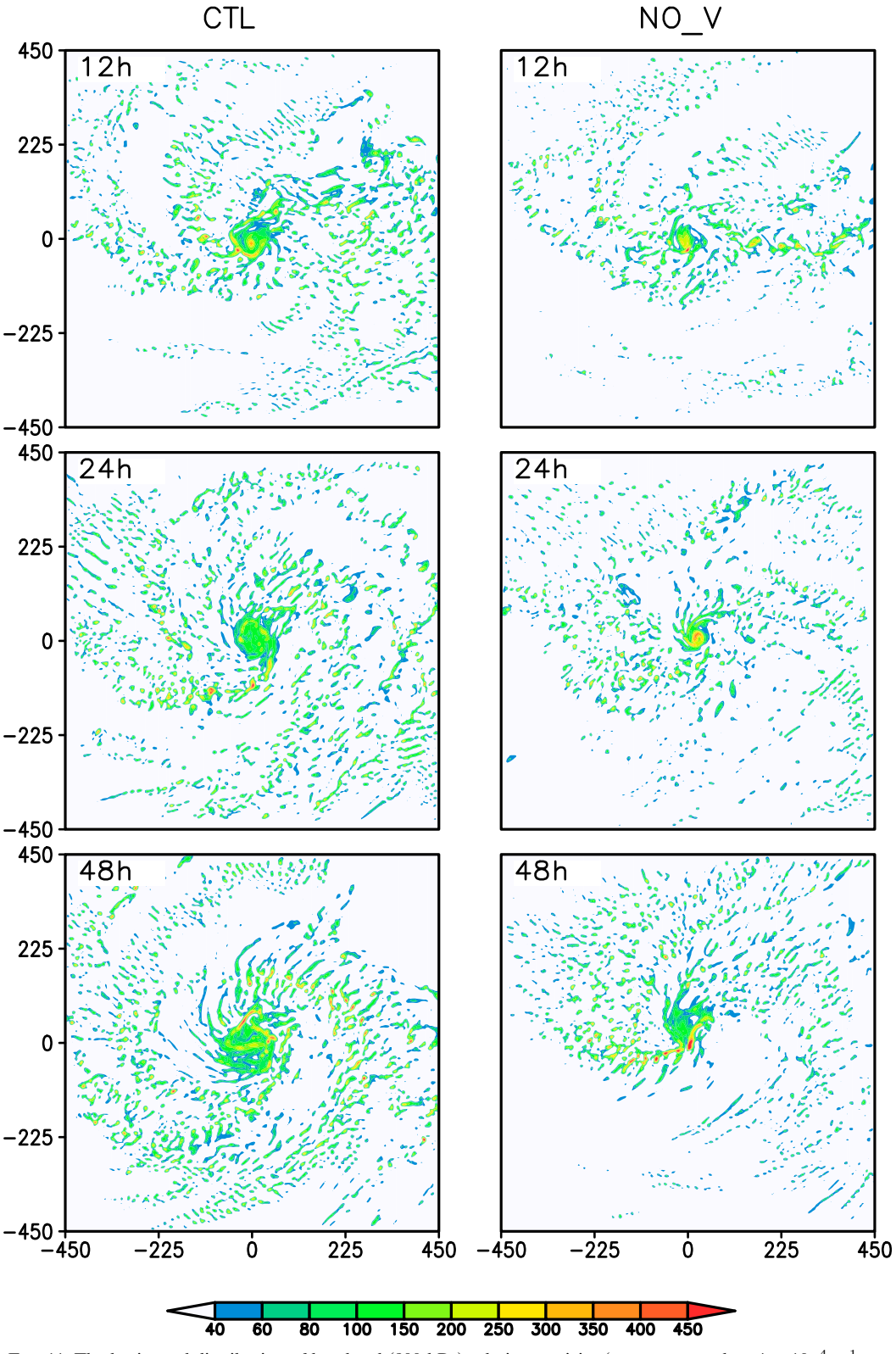

FIG. 11. The horizontal distribution of low-level (900-hPa) relative vorticity (areas greater than 4×10^{-4} s^{-1} are shaded) at hours (top) 12, (middle) 24, and (bottom) 48 in (left) CTL and (right) NO_V.

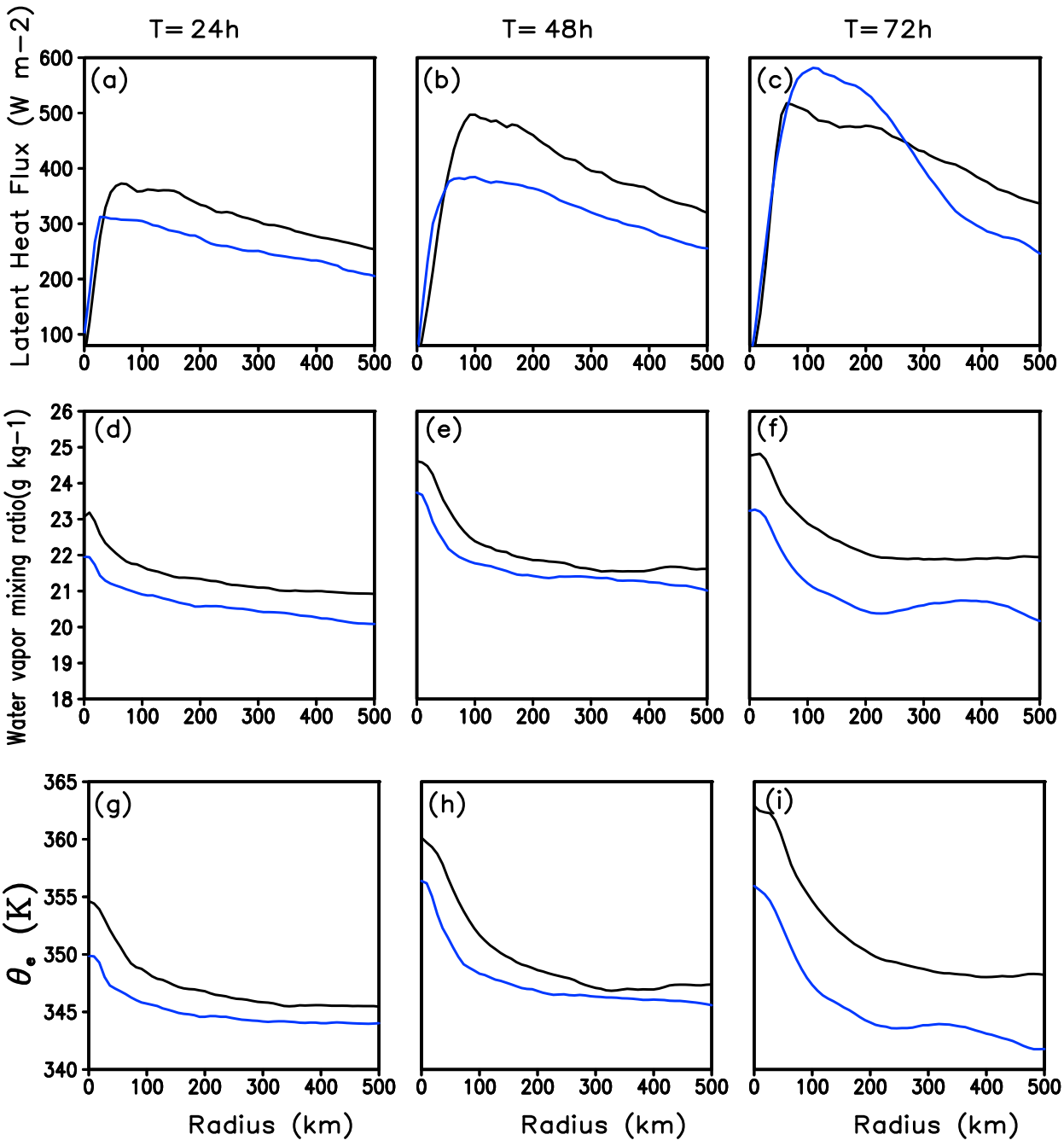

FIG. 12. Radial distributions of the azimuthal-mean (a)–(c) surface latent heat flux (W m^{-2}), (d)–(f) water vapor mixing ratio (g kg^{-1}) at 2 m, and (g)–(i) equivalent potential temperature θ_e (K) averaged over 0–2 km at hours (left) 24, (center) 48, and (right) 72 for the CTL (black) and NO_V (blue) experiments. A 24-h running mean has been applied to each panel.

The large-scale inflow converged these locally enhanced cyclonic vorticity cells, leading to the storm-scale circulation development.

It is interesting to note that in "NO_V" the convection appears to form mostly on the NW side, while in "CTL" it is more symmetric. This is likely directly related to the stronger shear shown in Fig. 9. Previous studies suggested that a stronger shear tended to create a larger wavenumber-1 asymmetry (e.g., Ge et al. 2013b).

The third process is through enhanced convective instability and the occurrence of spiral rainbands in the outer region. Because of the impact of the low-frequency cyclonic wind, the total surface wind speed increases in CTL. This leads to the increase of the surface latent heat flux (Figs. 12a–c). As a result,

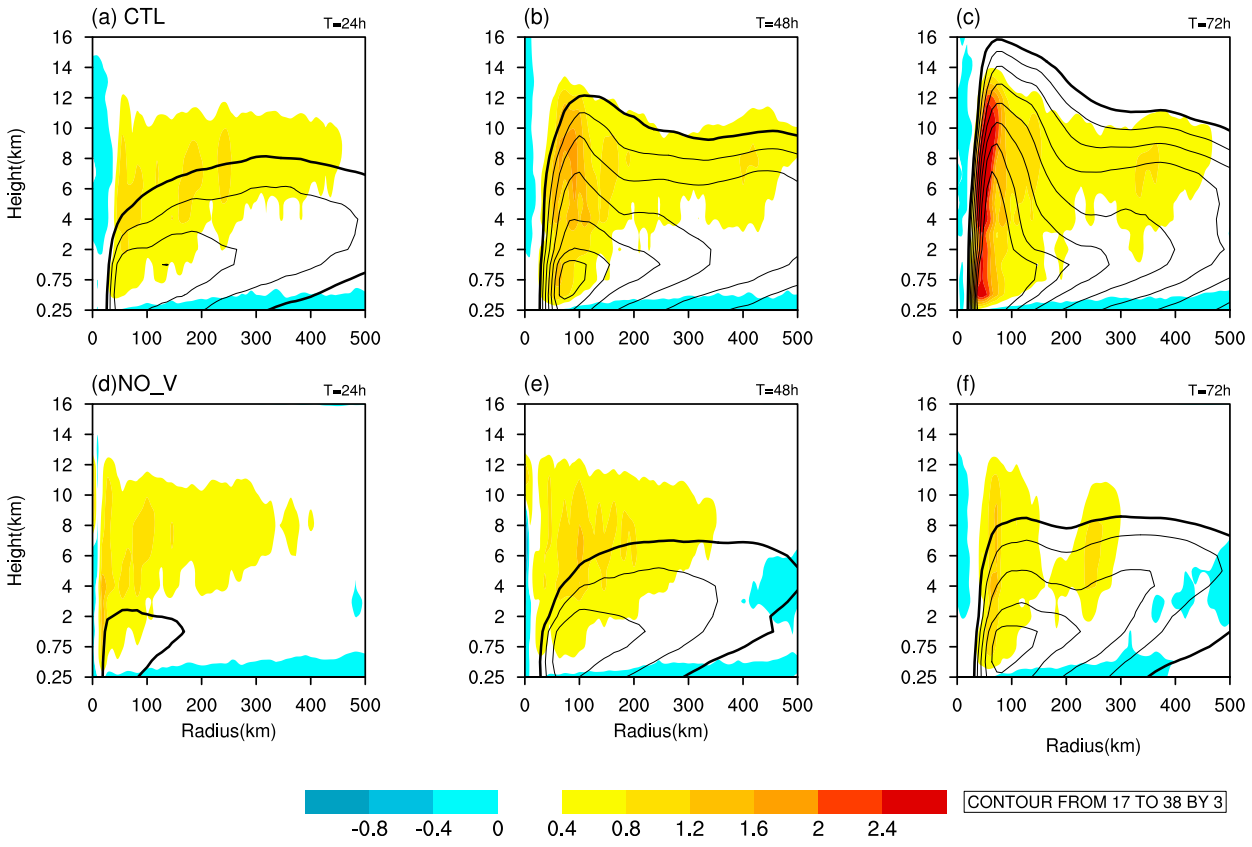

FIG. 13. Azimuthal mean vertical–radial cross sections of the tangential wind ($m\,s^{-1}$; contours) and the diabatic heating ($10^{-3}\,K\,s^{-1}$; shaded) fields at hours (left) 24, (center) 48, and (right) 72 from the (a)–(c) CTL and (d)–(f) NO_V experiments. A thickened black contour represents the wind speed of 17 $m\,s^{-1}$. A 24-h running mean has been applied to each panel.

there is a great increase of surface moisture in both the inner and outer regions (Figs. 12d–f). It is interesting to note that near-surface moisture increases more in the inner and the outer regions at hours 48 and 72, with a minimum in between (at about 300-km radius) (Figs. 12e,f). The increase of the moisture in the outer region eventually leads to a convectively unstable stratification, as seen from the radial profile of low-level equivalent potential temperature (Figs. 12g–i).

The enhanced convective activity in the outer region can be inferred from the vertical–radial distribution of the diabatic heating field (Fig. 13). Note that the diabatic heating in the upper troposphere, mostly attributed to condensational heating, expands more toward the outer region in CTL than in NO_V, particularly at hours 48 and 72. It was demonstrated that a radially expanded diabatic heating could enlarge the TC size through enhanced low-level inflow in the outer region (Xu and Wang 2010b). The expanded radial distribution of the diabatic heating is consistent with the vertical velocity field (Fig. 14), with stronger ascending motion appearing in the outer region (Figs. 14b,c,e,f). The vertical velocity difference field between CTL and NO_V shows enhanced ascending motion in both the eyewall and the outer region and a compensating descent in between (at about 300-km radius) (Figs. 14g–i).

It is physically argued that the enhanced convection and vertical motion in the outer region accelerate the low-level convergence in situ, causing a stronger inflow outside of the descent region. This helps accelerate the local tangential wind, leading to the expansion of the TC size. The strengthened local surface wind in the outer region further increases surface latent heat flux and thus near-surface moisture. Meanwhile the compensating descent near 300-km radius and associated anomalous low-level divergence prevents the inward transport of the moisture in the outer region. As a result, more moisture is accumulated in the outer region (Figs. 12d–f), leading to the setup of local convective instability (Figs. 12g–i) and convective bursts. Through this positive feedback loop between the local anomalous secondary circulation and the surface latent heat flux/moisture, an enlarged R17 difference occurs between CTL and NO_V.

It's worth mentioning that, while the descent near 300 km radius tends to reduce the low-level inflow slightly outside of this radius, favoring the accumulation of the moisture in the outer region, the TC intensity in CTL is still stronger than in NO_V. This is likely attributed to an enhanced secondary circulation in the inner-core region with strengthened ascent at the eyewall (Fig. 14i). Thus, the compensating descent near 300-km radius and associated anomalous low-level

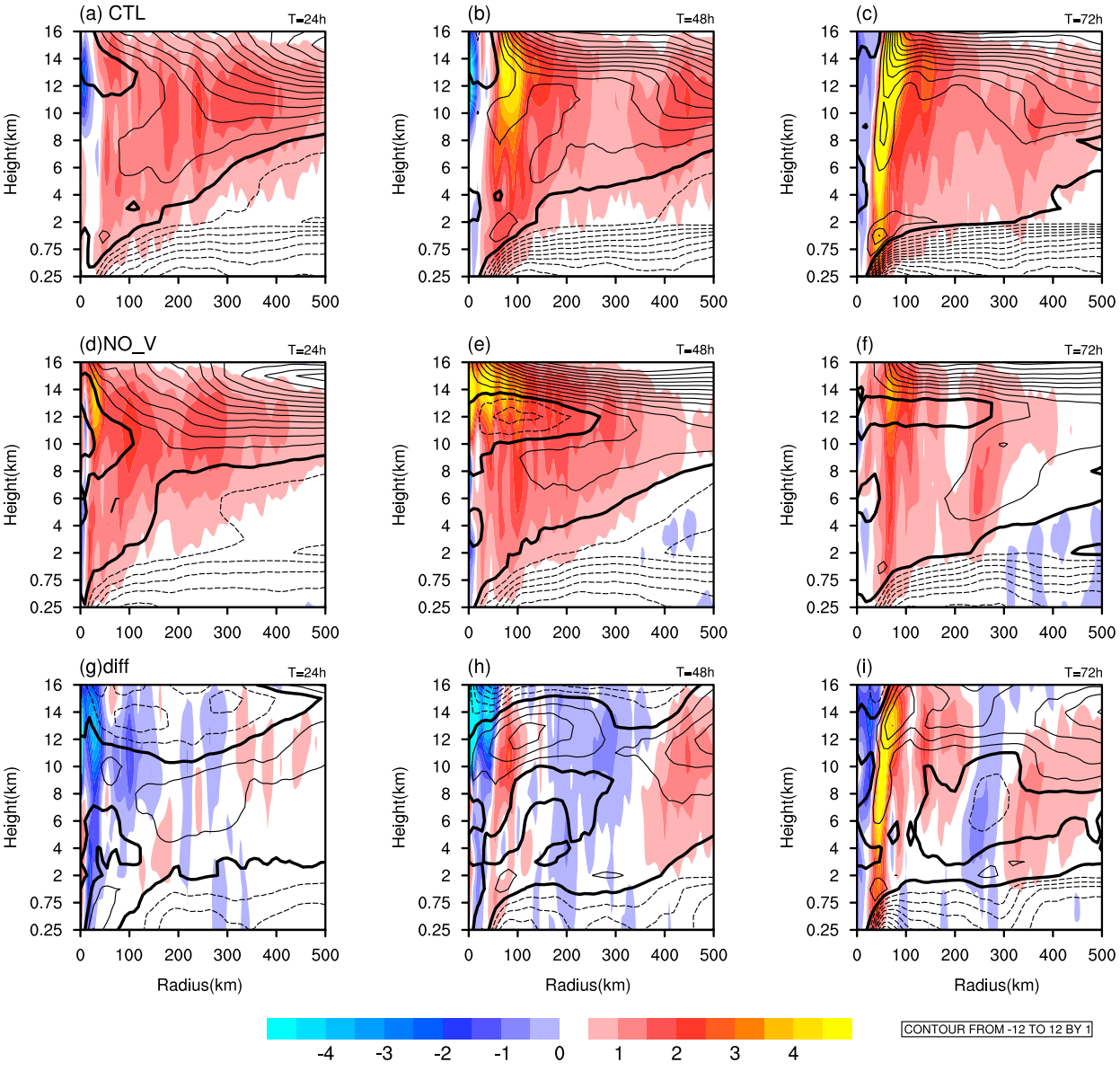

FIG. 14. Azimuthal mean vertical–radial cross sections of the radial wind (m s^{-1}; contours) and the vertical velocity (10^{-1} m s^{-1}; shaded, with red colors representing ascent motion) at hours (left) 24, (center) 48, and (right) 72 from (a)–(c) CTL, (d)–(f) NO_V, and (g)–(i) the difference between the two experiments (CTL − NO_V). A 24-h running mean has been applied to each panel.

divergence, on the one hand, strengthen the inflow in the inner-core and make the TC stronger, and on the other hand prevent the inward transport of the moisture in the outer region, leading to the accumulation of the surface moisture and thus convective instability in the outer region and the TC size increase.

6. Summary and discussion

Typhoon Lan (2017) was the largest tropical cyclone in the WNP in 2017. It caused a wide range of disasters and tremendous property loss to Japan. The physical mechanism responsible for its unusual size was investigated through a series of idealized numerical experiments with the WRF Model. It is found that a low-frequency large-scale cyclonic vortex accompanied Lan during its life cycle. In the control experiment (CTL) with all time-scale motions being included, the model is able to capture the observed unusual size of Lan. In the first sensitivity experiment (NO_ISO), the 10–90-day-filtered ISO fields including wind, temperature, specific humidity, geopotential height, and sea level pressure were removed from the initial and lateral boundary conditions. In the absence of the low-frequency impact, the TC size experiences a dramatic reduction. The size difference between CTL and NO_ISO indicates that the low-frequency ISO plays an important role in affecting the TC size.

To understand the relative role of the ISO dynamic and thermodynamic fields, two additional sensitivity experiments were conducted. They are same as CTL except that only the low-frequency wind (and associated pressure/temperature) field (NO_V) or only the low-frequency specific humidity field (NO_SH) was excluded, respectively. Comparing these experiments, we conclude that the low-frequency dynamic field contributes the most (~73%) to the TC size difference. Thus the idealized numerical model result suggests the dominant role of the low-frequency wind field in modulating the TC size.

A further analysis reveals that the low-frequency circulation affects the TC size through the following three processes. First, the low-frequency VWS tends to weaken the mean vertical shear, leading to a greater development of the initial vortex. A greater TC intensity is in general conductive to a larger TC size. Second, the low-frequency deep cyclonic vorticity promotes the merging of convective instability generated small-scale VHTs through a vorticity aggregation process. Through the enhanced vorticity aggregation process, a stronger, well-organized TC core structure forms, which leads to a faster growth of the TC intensity and size. Third, the low-frequency cyclonic wind strengthens the total surface wind speed and thus surface latent heat flux, increasing low-level moisture and convective instability in both the inner and outer regions. A compensating descent appears outside of the eyewall (near 300-km radius) as the TC secondary circulation develops. This descent tends to slow down the inward transport of the moisture from the outer region. As a result, the accumulated water vapor in the outer region triggers local convective bursts and promotes stronger radial inflow and tangential wind. The outer rainband strengthens the descent and an anomalous secondary circulation in the outer region. Through this positive feedback loop, more and stronger convective bursts appear in the outer region. The so-expanded radial profile of the diabatic heating eventually leads to a large TC size.

While previous studies paid less attention to the effect of the low-frequency circulation on TC size, here through idealized numerical model experiments, we demonstrate that the 10–90-day low-frequency flow plays an important role in modulating TC size. However, the current study is just a case study. Is there a statistical relationship between the low-frequency cyclonic circulation and TC size? To address this question, we examined the general relationship between TC size and ISO intensity in the WNP during an 18-yr period (2001–18). Figure 15 shows a scatter diagram between them. Here the TC size is defined as R17 when a TC reaches a maximum intensity, and the ISO intensity is represented by standardized 10–90-day-filtered outgoing longwave radiation (OLR) anomalies averaged at a 10° by 10° box over the TC center during the time of the maximum intensity. The number of total TC cases analyzed here is 334. Note that there is a statistically significant relationship between the TC size and the ISO strength. A stronger ISO intensity (i.e., a larger negative OLR anomaly) is often associated with a greater TC size. The statistical relationship greatly supports the conclusion from the current case study, that is, the low-frequency cyclonic vortex associated with the ISO plays an important role in causing the large TC

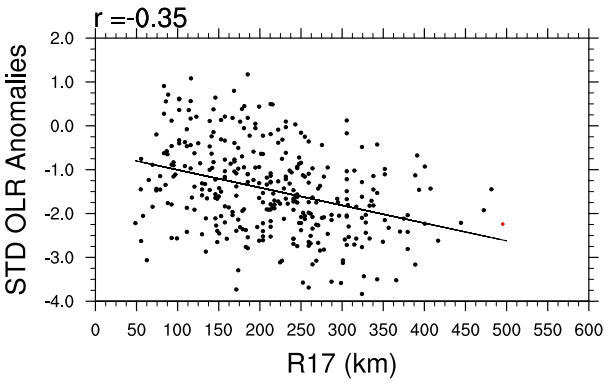

FIG. 15. Scatter diagram of TC size (R17; km) at the time of maximum TC intensity and corresponding ISO intensity (represented by the standardized 10–90-day-filtered OLR anomaly averaged at a 10° by 10° box over the TC center during the time of the maximum intensity) in the WNP during 2001–18. The red dot represents TC Lan (2017). The correlation coefficient is significant at a 95% confidence level.

size for Lan (2017). In Fig. 15 the TC size during its maximum intensity was used. A parallel analysis with the use of a maximum TC size during its life cycle shows a similar significant relationship with the ISO strength (figure not shown).

For the life cycle of an individual TC, the relationship between its size and intensity with time appears more complicated. For example, one can see from Fig. 4 that there is a closer link between Lan's intensity and size during its initial developing stage, but their relationship becomes more complicated during the later mature stage. In an idealized numerical experiment, Kilroy et al. (2016) showed that TC enlarges its size during its initial developing stage and continues growing in size even after it starts decaying. Sitkowski et al. (2011) and Zhou and Wang (2011) found that the secondary eyewall formation was conducive to the expansion of TC outer region, but the subsequent eyewall replacement cycle would weaken TC inner-core intensity, causing intensity fluctuation. Therefore, it is important to conduct further observational and modeling studies to reveal the complicated, temporally varying relationship between TC intensity and size.

Acknowledgments. This study is jointly supported by NSFC Grant 42088101, NSF Grant AGS-16-43297, and NOAA Grant NA18OAR4310298. This is SOEST Contribution Number 11202, IPRC Contribution Number 1491, and ESMC Contribution Number 340. The numerical calculations in this paper have been done on the supercomputing system in the Supercomputing Center of Nanjing University of Information Science and Technology.

Data availability statement. The OLR data were provided by the NOAA Climate Diagnostics Center (CDC) (http://www.cdc.noaa.gov). The Multiplatform Tropical Cyclone Surface Wind Analysis (MTCSWA) product was obtained from the National Environmental Satellite Data and Information Service (NESDIS) (http://www.nesdis.noaa.gov). The reanalysis

data were provided by the National Centers for Environmental Prediction (NCEP) final (FNL) analysis. The data of statistical TCs was provided by the Joint Typhoon Warning Center (JTWC) (https://www.metoc.navy.mil/jtwc/jtwc.html).

REFERENCES

Atkinson, G. D., 1971: Forecaster's guide to tropical meteorology. Air Weather Service Tech. Rep. 240, 295 pp.

Beljaars, A. C. M., 1995: The parameterization of surface fluxes in large-scale models under free convection. *Quart. J. Roy. Meteor. Soc.*, **121**, 255–270, https://doi.org/10.1002/qj.49712152203.

Bi, M. Y., T. Li, M. Peng, and X. Y. Shen, 2015: Interactions between typhoon Megi (2010) and a low-frequency monsoon gyre. *J. Atmos. Sci.*, **72**, 2682–2702, https://doi.org/10.1175/JAS-D-14-0269.1.

Cao, X., T. Li, M. Peng, W. Chen, and G.-H. Chen, 2014: Effects of monsoon trough intraseasonal oscillation on tropical cyclogenesis over the western North Pacific. *J. Atmos. Sci.*, **71**, 4639–4660, https://doi.org/10.1175/JAS-D-13-0407.1.

Carr, L. E., and R. L. Elsberry, 1997: Models of tropical cyclone wind distribution and beta-effect propagation for application to tropical cyclone track forecasting. *Mon. Wea. Rev.*, **125**, 3190–3209, https://doi.org/10.1175/1520-0493(1997)125<3190:MOTCWD>2.0.CO;2.

Chan, K. T. F., and J. C. L. Chan, 2012: Size and strength of tropical cyclones as inferred from QuikSCAT data. *Mon. Wea. Rev.*, **140**, 811–824, https://doi.org/10.1175/MWR-D-10-05062.1.

——, and ——, 2014: Impacts of initial vortex size and planetary vorticity on tropical cyclone size. *Quart. J. Roy. Meteor. Soc.*, **140**, 2235–2248, https://doi.org/10.1002/qj.2292.

Charnock, H., 1955: Wind stress on a water surface. *Quart. J. Roy. Meteor. Soc.*, **81**, 639–640, https://doi.org/10.1002/qj.49708135027.

Chavas, D. R., and K. A. Emanuel, 2010: A QuikSCAT climatology of tropical cyclone size. *Geophys. Res. Lett.*, **37**, L18816, https://doi.org/10.1029/2010GL044558.

Cocks, S. B., and W. M. Gray, 2002: Variability of the outer wind profiles of western North Pacific typhoons: Classifications and techniques for analysis and forecasting. *Mon. Wea. Rev.*, **130**, 1989–2005, https://doi.org/10.1175/1520-0493(2002)130<1989:VOTOWP>2.0.CO;2.

Davis, C., and Coauthors, 2008: Prediction of landfalling hurricanes with the advanced Hurricane WRF Model. *Mon. Wea. Rev.*, **136**, 1990–2005, https://doi.org/10.1175/2007MWR2085.1.

——, 2015: The formation of moist vortices and tropical cyclones in idealized simulations. *J. Atmos. Sci.*, **72**, 3499–3516, https://doi.org/10.1175/JAS-D-15-0027.1.

DeMaria, M., and J. Kaplan, 1994: A Statistical Hurricane Intensity Prediction Scheme (SHIPS) for the Atlantic basin. *Wea. Forecasting*, **9**, 209–220, https://doi.org/10.1175/1520-0434(1994)009<0209:ASHIPS>2.0.CO;2.

Duchon, C. E., 1979: Lanczos filtering in one and two dimensions. *J. Appl. Meteor.*, **18**, 1016–1022, https://doi.org/10.1175/1520-0450(1979)018<1016:LFIOAT>2.0.CO;2.

Dudhia, J., 1989: Numerical study of convection observed during the Winter Monsoon Experiment using a mesoscale two–dimensional model. *J. Atmos. Sci.*, **46**, 3077–3107, https://doi.org/10.1175/1520-0469(1989)046<3077:NSOCOD>2.0.CO;2.

Emanuel, K., 2005: Increasing destructiveness of tropical cyclones over the past 30 years. *Nature*, **436**, 686–688, https://doi.org/10.1038/nature03906.

Frank, W. M., and W. M. Gray, 1980: Radius and frequency of 15 (30 kt) winds around tropical cyclones. *J. Appl. Meteor.*, **19**, 219–223, https://doi.org/10.1175/1520-0450(1980)019<0219:RAFOMS>2.0.CO;2.

Frisius, T., 2015: What controls the size of a tropical cyclone? Investigations with an axisymmetric model. *Quart. J. Roy. Meteor. Soc.*, **141**, 2457–2470, https://doi.org/10.1002/qj.2537.

Fu, B., T. Li, M. S. Peng, and F. Weng, 2007: Analysis of tropical cyclogenesis in the western North Pacific for 2000 and 2001. *Wea. Forecasting*, **22**, 763–780, https://doi.org/10.1175/WAF1013.1.

Ge, X. Y., T. Li, and S. M. Peng, 2013a: Tropical cyclone genesis efficiency: Mid-level versus bottom vortex. *J. Trop. Meteor.*, **19**, 197–213.

——, ——, and ——, 2013b: Effects of vertical shears and mid-level dry air on tropical cyclone developments. *J. Atmos. Sci.*, **70**, 3859–3875, https://doi.org/10.1175/JAS-D-13-066.1.

——, W. Xu, and S. W. Zhou, 2015: Sensitivity of tropical cyclone intensification to inner-core structure. *Adv. Atmos. Sci.*, **32**, 1407–1418, https://doi.org/10.1007/s00376-015-4286-5.

Gray, W. M., 1968: Global view of the origin of tropical disturbances and storms. *Mon. Wea. Rev.*, **96**, 669–700, https://doi.org/10.1175/1520-0493(1968)096<0669:GVOTOO>2.0.CO;2.

Hanley, D. E., J. Molinari, and D. Keyser, 2001: A composite study of the interactions between tropical cyclones and upper-tropospheric troughs. *Mon. Wea. Rev.*, **129**, 2570–2584, https://doi.org/10.1175/1520-0493(2001)129<2570:ACSOTI>2.0.CO;2.

Harr, P. A., R. L. Elsberry, and J. C. Chan, 1996: Transformation of a large monsoon depression to a tropical storm during TCM-93. *Mon. Wea. Rev.*, **124**, 2625–2643, https://doi.org/10.1175/1520-0493(1996)124<2625:TOALMD>2.0.CO;2.

Hill, K. A., and G. M. Lackmann, 2009: Influence of environmental humidity on tropical cyclone size. *Mon. Wea. Rev.*, **137**, 3294–3315, https://doi.org/10.1175/2009MWR2679.1.

Holland, G. J., and R. T. Merrill, 1984: On the dynamics of tropical cyclone structural changes. *Quart. J. Roy. Meteor. Soc.*, **110**, 723–745, https://doi.org/10.1002/qj.49711046510.

Hong, S. Y., and J. O. J. Lim, 2006: The WRF single-moment 6-class microphysics scheme (WSM6). *J. Korean Meteor. Soc.*, **42**, 129–151.

——, Y. Noh, and J. Dudhia, 2006: A new vertical diffusion package with an explicit treatment of entrainment processes. *Mon. Wea. Rev.*, **134**, 2318–2341, https://doi.org/10.1175/MWR3199.1.

Hsu, P. C., T. Li, and C.-H. Tsou, 2011: Interactions between boreal summer intraseasonal oscillations and synoptic-scale disturbances over the western North Pacific. Part I: Energetics diagnosis. *J. Climate*, **24**, 927–941, https://doi.org/10.1175/2010JCLI3833.1.

Irish, J. L., D. T. Resio, and J. J. Ratcliff, 2008: The influence of storm size on hurricane surge. *J. Phys. Oceanogr.*, **38**, 2003–2013, https://doi.org/10.1175/2008JPO3727.1.

Jones, S. C., 1995: The evolution of vortices in vertical shear. I: Initially barotropic vortices. *Quart. J. Roy. Meteor. Soc.*, **121**, 821–851, https://doi.org/10.1002/qj.49712152406.

——, 2000: The evolution of vortices in vertical shear. II: Large-scale asymmetries. *Quart. J. Roy. Meteor. Soc.*, **126**, 3137–3159, https://doi.org/10.1002/qj.49712657008.

Kain, J. S., and J. M. Fritsch, 1993: Convective parameterization for mesoscale models: The Kain–Fritsch scheme. *The Representation of Cumulus Convection in Numerical Models, Meteor. Monogr.*, No. 24, Amer. Meteor. Soc., 165–170.

Kilroy, G., and R. K. Smith, 2016: A numerical study of deep convection in tropical cyclones. *Quart. J. Roy. Meteor. Soc.*, **142**, 3138–3151, https://doi.org/10.1002/qj.2895.

——, and ——, 2017: The effects of initial vortex size on tropical cyclogenesis and intensification. *Quart. J. Roy. Meteor. Soc.*, **143**, 2832–2845, https://doi.org/10.1002/qj.3134.

——, ——, and M. T. Montgomery, 2016: Why do model tropical cyclones grow progressively in size and decay in intensity after reaching maturity? *J. Atmos. Sci.*, **73**, 487–503, https://doi.org/10.1175/JAS-D-15-0157.1.

——, ——, and ——, 2017: A unified view of tropical cyclogenesis and intensification. *Quart. J. Roy. Meteor. Soc.*, **143**, 450–462, https://doi.org/10.1002/qj.2934.

Kimball, S. K., and M. S. Mulekar, 2004: A 15-year climatology of North Atlantic tropical cyclones. Part I: Size parameters. *J. Climate*, **17**, 3555–3575, https://doi.org/10.1175/1520-0442(2004)017<3555:AYCONA>2.0.CO;2.

Knaff, J. A., M. DeMaria, D. A. Molenar, C. R. Sampson, and M. G. Seybold, 2011: An automated, objective, multiple-satellite-platform tropical cyclone surface wind analysis. *J. Appl. Meteor. Climatol.*, **50**, 2149–2166, https://doi.org/10.1175/2011JAMC2673.1.

——, S. P. Longmore, and D. A. Molenar, 2014: An objective satellite-based tropical cyclone size climatology. *J. Climate*, **27**, 455–476, https://doi.org/10.1175/JCLI-D-13-00096.1.

——, C. J. Slocum, K. D. Musgrave, C. R. Sampson, and B. R. Strahl, 2016: Using routinely available information to estimate tropical cyclone wind structure. *Mon. Wea. Rev.*, **144**, 1233–1247, https://doi.org/10.1175/MWR-D-15-0267.1.

Lander, M., 1994: Description of a monsoon gyre and its effects on the tropical cyclones in the western North Pacific during August 1991. *Wea. Forecasting*, **9**, 640–654, https://doi.org/10.1175/1520-0434(1994)009<0640:DOAMGA>2.0.CO;2.

Li, R. C. Y., and W. Zhou, 2013a: Modulation of western North Pacific tropical cyclone activity by the ISO. Part I: Genesis and intensity. *J. Climate*, **26**, 2904–2918, https://doi.org/10.1175/JCLI-D-12-00210.1.

——, and ——, 2013b: Modulation of western North Pacific tropical cyclone activity by the ISO. Part II: Tracks and landfalls. *J. Climate*, **26**, 2919–2930, https://doi.org/10.1175/JCLI-D-12-00211.1.

Li, T., 2012: Synoptic and climatic aspects of tropical cyclogenesis in western North Pacific. *Cyclones: Formation, Triggers and Control*, K. Oouchi and H. Fudeyasu, Eds., Nova Science Publishers, 61–94.

——, 2014: Recent advance in understanding the dynamics of the Madden–Julian oscillation. *J. Meteor. Res.*, **28**, 1–33, https://doi.org/10.1007/s13351-014-3087-6.

——, and B. Wang, 2005: A review on the western North Pacific monsoon: Synoptic-to-interannual variabilities. *Terr. Atmos. Oceanic Sci.*, **16**, 285–314, https://doi.org/10.3319/TAO.2005.16.2.285(A).

——, X. Ge, B. Wang, and Y. Zhu, 2006: Tropical cyclogenesis associated with Rossby wave energy dispersion of a preexisting typhoon. Part II: Numerical simulations. *J. Atmos. Sci.*, **63**, 1390–1409, https://doi.org/10.1175/JAS3693.1.

Liebmann, B., H. H. Hendon, and J. D. Glick, 1994: The relationship between tropical cyclones of the western Pacific and Indian Oceans and the Madden–Julian oscillation. *J. Meteor. Soc. Japan*, **72**, 401–412, https://doi.org/10.2151/jmsj1965.72.3_401.

Liu, K. S., and J. C. L. Chan, 2002: Synoptic flow patterns associated with small and large tropical cyclones over the western North Pacific. *Mon. Wea. Rev.*, **130**, 2134–2142, https://doi.org/10.1175/1520-0493(2002)130<2134:SFPAWS>2.0.CO;2.

Ma, C., M. Peng, T. Li, Y. Sun, J. Liu, and M. Bi, 2019: Effects of background state on tropical cyclone size over the western North Pacific and northern Atlantic. *Climate Dyn.*, **52**, 4143–4156, https://doi.org/10.1007/s00382-018-4372-3.

Maloney, E. D., and D. L. Hartmann, 1998: Frictional moisture convergence in a composite life cycle of the Madden–Julian oscillation. *J. Climate*, **11**, 2387–2403, https://doi.org/10.1175/1520-0442(1998)011<2387:FMCIAC>2.0.CO;2.

Merrill, R. T., 1984: A comparison of large and small tropical cyclones. *Mon. Wea. Rev.*, **112**, 1408–1418, https://doi.org/10.1175/1520-0493(1984)112<1408:ACOLAS>2.0.CO;2.

Mlawer, E., S. J. Taubman, P. D. Brown, M. J. Iacono, and S. A. Clough, 1997: Radiative transfer for inhomogeneous atmospheres: RRTM, a validated correlated-*k* model for the longwave. *J. Geophys. Res.*, **102**, 16 663–16 682, https://doi.org/10.1029/97JD00237.

Montgomery, M. T., and Coauthors, 2012: The Pre-depression Investigation of Cloud systems in the Tropics (PREDICT) experiment: Scientific basis, new analysis tools, and some first results. *Bull. Amer. Meteor. Soc.*, **93**, 153–172, https://doi.org/10.1175/BAMS-D-11-00046.1.

Nolan, D. S., 2007: What is the trigger for tropical cyclogenesis? *Aust. Meteor. Mag.*, **56**, 241–266.

——, and M. G. McGauley, 2012: Tropical cyclogenesis in wind shear: Climatological relationships and physical processes. *Cyclones: Formation, Triggers, and Control*, K. Oouchi and H. Fudeyasu, Eds., Nova Science, 1–34.

Ritchie, E. A., and G. J. Holland, 1999: Large-scale patterns associated with tropical cyclogenesis in the western Pacific. *Mon. Wea. Rev.*, **127**, 2027–2043, https://doi.org/10.1175/1520-0493(1999)127<2027:LSPAWT>2.0.CO;2.

Rotunno, R., and K. A. Emanuel, 1987: An air–sea interaction theory for tropical cyclones. Part II: Evolutionary study using a nonhydrostatic axisymmetric numerical model. *J. Atmos. Sci.*, **44**, 542–561, https://doi.org/10.1175/1520-0469(1987)044<0542:AAITFT>2.0.CO;2.

Sitkowski, M., J. P. Kossin, and C. M. Rozoff, 2011: Intensity and structure changes during hurricane eyewall replacement cycles. *Mon. Wea. Rev.*, **139**, 3829–3847, https://doi.org/10.1175/MWR-D-11-00034.1.

Skamarock, W. C., and Coauthors, 2008: A description of the Advanced Research WRF version 3. NCAR Tech. Note NCAR/TN-475+STR, 113 pp., https://doi.org/10.5065/D68S4MVH.

Smith, R. K., C. W. Schmidt, and M. T. Montgomery, 2011: An investigation of rotational influences on tropical-cyclone size and intensity. *Quart. J. Roy. Meteor. Soc.*, **137**, 1841–1855, https://doi.org/10.1002/qj.862.

Sun, Y., and Coauthors, 2017: Impact of ocean warming on tropical cyclone size and its destructiveness. *Sci. Rep.*, **7**, 8154, https://doi.org/10.1038/s41598-017-08533-6.

Tsuji, H., H. Itoh, and K. Nakajima, 2016: Mechanism governing the size change of tropical cyclone-like vortices. *J. Meteor. Soc. Japan*, **94**, 219–236, https://doi.org/10.2151/jmsj.2016-012.

Wang, Y., and G. J. Holland, 1996: Tropical cyclone motion and evolution in vertical shear. *J. Atmos. Sci.*, **53**, 3313–3332, https://doi.org/10.1175/1520-0469(1996)053<3313:TCMAEI>2.0.CO;2.

Weatherford, C. L., and W. M. Gray, 1988: Typhoon structure as revealed by aircraft reconnaissance. Part I: Data analysis and climatology. *Mon. Wea. Rev.*, **116**, 1032–1043, https://doi.org/10.1175/1520-0493(1988)116<1032:TSARBA>2.0.CO;2.

Wu, L., H. Zong, and J. Liang, 2013: Observational analysis of tropical cyclone formation associated with monsoon gyres.

J. Atmos. Sci., **70**, 1023–1034, https://doi.org/10.1175/JAS-D-12-0117.1.

——, W. Tian, Q. Liu, and J. Cao, 2015: Implications of the observed relationship between tropical cyclone size and intensity over the western North Pacific. *J. Climate*, **28**, 9501–9506, https://doi.org/10.1175/JCLI-D-15-0628.1.

Xu, J., and Y. Wang, 2010a: Sensitivity of the simulated tropical cyclone inner-core size to the initial vortex size. *Mon. Wea. Rev.*, **138**, 4135–4157, https://doi.org/10.1175/2010MWR3335.1.

——, and ——, 2010b: Sensitivity of tropical cyclone inner core size and intensity to the radial distribution of surface entropy flux. *J. Atmos. Sci.*, **67**, 1831–1852, https://doi.org/10.1175/2010JAS3387.1.

Xu, Y. M., T. Li, and M. Peng, 2013: Tropical cyclogenesis in the western North Pacific as revealed by the 2008–09 YOTC data. *Wea. Forecasting*, **28**, 1038–1056, https://doi.org/10.1175/WAF-D-12-00104.1.

——, ——, and ——, 2014: Roles of the synoptic-scale wave train, the intraseasonal oscillation, and high-frequency eddies in the genesis of Typhoon Manyi (2001). *J. Atmos. Sci.*, **71**, 3706–3722, https://doi.org/10.1175/JAS-D-13-0406.1.

Yan, Z. Y., X. Ge, M. S. Peng, and T. Li, 2019: Does monsoon gyre always favor tropical cyclone rapid intensification? *Quart. J. Roy. Meteor. Soc.*, **145**, 2685–2697, https://doi.org/10.1002/qj.3586.

Yang, L., Y. Du, D. Wang, C. Wang, and X. Wang, 2015: Impact of intraseasonal oscillation on the tropical cyclone track in the South China Sea. *Climate Dyn.*, **44**, 1505–1519, https://doi.org/10.1007/s00382-014-2180-y.

Zhao, C., and T. Li, 2018: Basin dependence of the MJO modulating tropical cyclone genesis. *Climate Dyn.*, **52**, 6081–6096, https://doi.org/10.1007/s00382-018-4502-y.

Zhou, C., and T. Li, 2010: Upscale feedback of tropical synoptic variability to intraseasonal oscillations through the nonlinear rectification of the surface latent heat flux. *J. Climate*, **23**, 5738–5754, https://doi.org/10.1175/2010JCLI3468.1.

Zhou, X., and B. Wang, 2011: Mechanism of concentric eyewall replacement cycles and associated intensity change. *J. Atmos. Sci.*, **68**, 972–988, https://doi.org/10.1175/2011JAS3575.1.